Engineering Geology 297 (2022) 106530

Contents lists available at ScienceDirect

Engineering Geology

journal homepage: www.elsevier.com/locate/enggeo

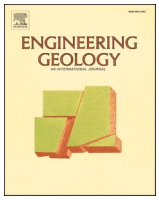

# Inferring subsidence characteristics in Wuhan (China) through multitemporal InSAR and hydrogeological analysis

Jiyuan Hu [a,b,e,g], Mahdi Motagh [c,d], Jiming Guo [f,*], Mahmud Haghshenas Haghighi [d], Tao Li [h], Fen Qin [a,b,e], Wenhao Wu [i]

[a] College of Geography and Environmental Science, Henan University, Kaifeng 475004, China
[b] Key Laboratory of Geospatial Technology for the Middle and Lower Yellow River Regions, Henan University, Ministry of Education, Kaifeng 475004, China
[c] Helmholtz Centre Potsdam, GFZ German Research Centre for Geosciences, Potsdam 14473, Germany
[d] Institute of Photogrammetry and GeoInformation, Leibniz University Hannover, 30167 Hannover, Germany
[e] Henan Industrial Technology Academy of Spatial-Temporal Big Data, Henan University, Zhengzhou 450046, China
[f] School of Geodesy and Geomatics, Wuhan University, Wuhan 430079, China
[g] Henan Technology Innovation Center of Spatio-Temporal Big Data, Henan University, Zhengzhou 450046, China
[h] GNSS Research Center, Wuhan University, Wuhan 430079, China
[i] Hunan Province Key Laboratory of Coal Resources Clean-utilization and Mine Environment Protection, Hunan University of Science and Technology, Xiangtan 411201, China

ARTICLE INFO

*Keywords:*
Consolidation subsidence
Karst collapse
Multitemporal InSAR
Wuhan

ABSTRACT

Wuhan (China) is facing severe consolidation subsidence of soft soil and karst collapse hazards. To quantitatively explore the extent and causes of land subsidence in Wuhan, we performed multitemporal interferometry (MTI) analysis using synthetic aperture radar (SAR) data from the TerraSAR-X satellite from 2013 to 2017 and the Sentinel-1A satellite from 2015 to 2017. MTI results reveal four major subsidence zones in Wuhan, namely, Hankou (exceeding −6 cm/yr), Xudong-Qingshan (−3 cm/yr), Baishazhou-Jiangdi (−3 cm/yr), and Jianshe-Yangluo (−2 cm/yr). Accuracy assessment using 106 levelling benchmarks and cross-validation between the two InSAR-based results indicate an overall root-mean-square error (RMSE) of 2.5 and 3.1 mm/yr, respectively. Geophysical and geological analyses suggest that among the four major subsiding zones, Hankou, Xudong-Qingshan, and Jianshe-Yangluo are located in non-karstic soft soil areas, where shallow groundwater (< 30 m) declines driven by engineering dewatering and industrial water depletion contribute directly to soft soil compaction. Subsidence in the Baishazhou-Jiangdi zone develops in the karst terrain with abundant underground caves and fissures, which are major natural factors for gradual subsidence and karst collapse. Spatial variation analysis of the geological conditions indicates that the stage of karst development plays the most important role in influencing kart subsidence, followed by municipal construction, proximity to major rivers, and overlying soil structure. Moreover, land subsidence in this zone is affected more via coupling effects from multiple factors. Risk zoning analysis integrating subsidence horizontal gradient, InSAR deformation rates, and municipal construction density show that the high-risk areas in Wuhan are mainly distributed in the Tianxingzhou and Baishazhou-Jiangdi zone, and generally spread along the metro lines.

## 1. Introduction

Land subsidence is a gradual settling or sudden sinking of the Earth's surface due to the removal or displacement of subsurface earth materials, occurring in more than 150 countries and nearly 1600 of the world's major cities (Bagheri-Gavkosh et al., 2021; Perkins, 2021; Herrera-García et al., 2021). Wuhan (China), with a population of over 12 million, is undergoing massive municipal construction, and more than forty communities are suffering from severe land subsidence. Moreover, six karst zones strike WNW-ESE through the central city, rendering it one of the few megacities to suffer from another mechanism of land subsidence, which is karst collapse.

Commonly used in situ monitoring or investigation methods for land subsidence and karst collapse include levelling, GPS, ground-

* Corresponding author.
*E-mail address:* 40150028@henu.edu.cn (J. Guo).

https://doi.org/10.1016/j.enggeo.2022.106530
Received 16 December 2020; Received in revised form 7 January 2022; Accepted 10 January 2022
Available online 13 January 2022

penetrating radar, and trenching. These methods are highly targeted and reliably accurate for monitoring or investigating land subsidence at a single point or local areas but are extremely limited in space (Motagh et al., 2007; Bonetto et al., 2008; Dahm et al., 2010; Gutiérrez et al., 2012). In particular, Wuhan is built on a dispersed karst zones (Fig. 1). Frequent geomorphic expression changes due to intensive urban construction and natural processes make object-contacted (or even destructive) in situ monitoring or investigation methods inefficient for mapping dispersed karst collapse and large-scale subsidence (Galve et al., 2015). Multitemporal InSAR techniques, such as Persistent Scatterer Interferometry (PSI) (Ferretti et al., 2001) and the Small Baseline Subset (SBAS) method (Berardino et al., 2002), are effective in detecting subtle displacements in large-scale areas with millimetre-level accuracy. They are also used to map and characterize land subsidence in karst geological environments (e.g., Gutiérrez et al., 2012; Ng et al., 2018; Kim et al., 2019).

Several studies used PSI or SBAS to monitor spatial–temporal evolutionary characteristics of land deformation in Wuhan and analyse its causes from a qualitative point of view (Bai et al., 2017; Zhou et al., 2017; Zhang et al., 2019). More recently, Han et al. (2020) investigated land deformation in Wuhan for two time periods, from 2007 to 2010 and from, 2015 to 2019, by processing three tracks of SAR data from ALOS-1 (January 2007–October 2010), ENVISAT (December 2008–May 2010), and Sentinel-1A (April 2015–June 2019). The latest study by Jiang et al. (2021) analysed land subsidence in Wuhan from 2012 to 2019 using COSMO-SkyMed data. However, the coupling effects of multiple influencing factors affecting karst collapse in the Baishazhou-Jiangdi zone remains underexplored. In this work, we extended the land subsidence studies in Wuhan by using more SAR data from TerraSAR-X and Sentinel-1A, exploited a large number of hydrological datasets for the detailed interpretation of land subsidence, and assessed driving factors for the karst subsidence based on spatial variation analysis of the geological conditions, the so-called geographical detector-based approach (Wang et al., 2010). Moreover, a risk map was developed

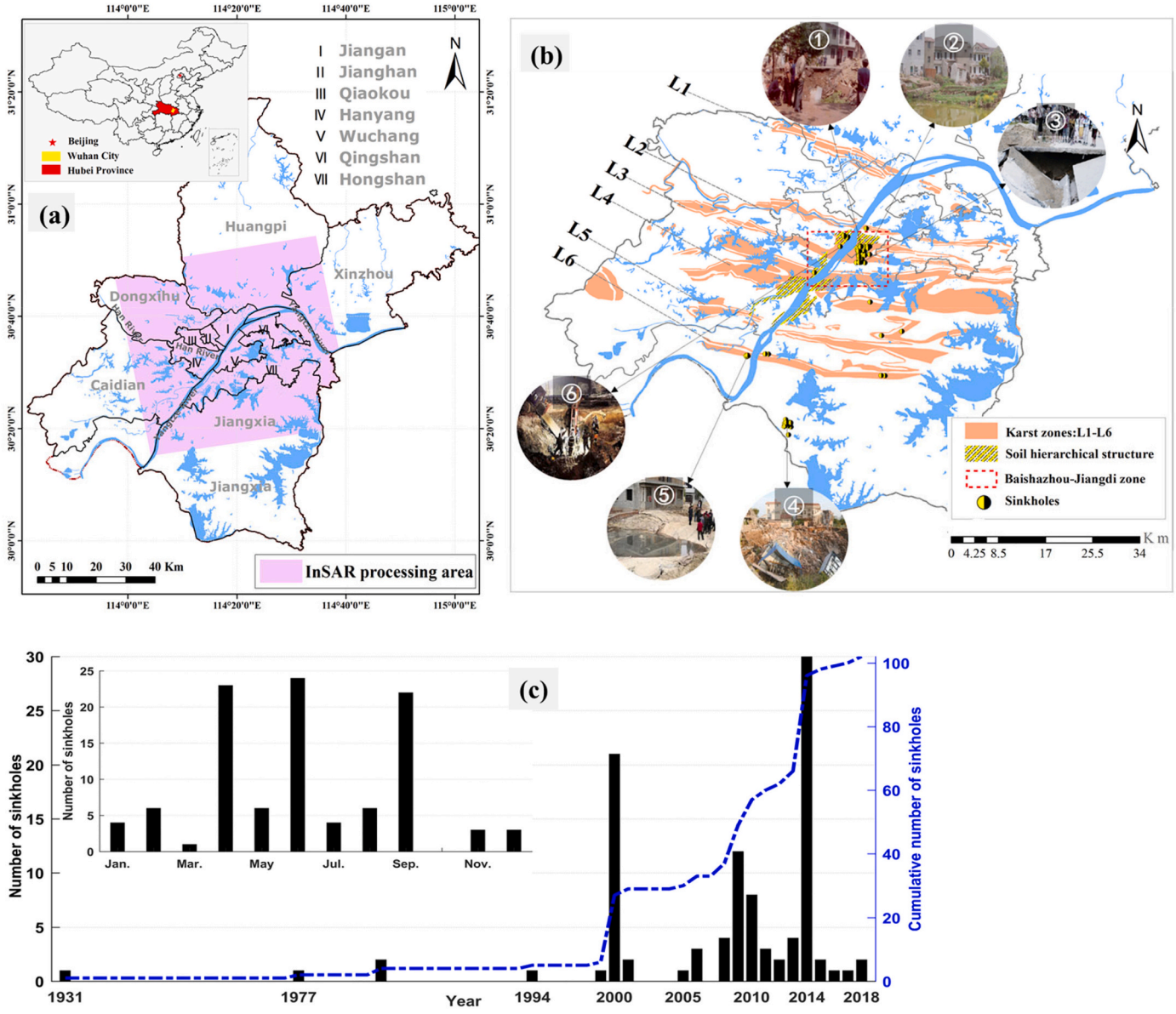


**Fig. 1.** (a) Location and coverage of the study area. Roman numerals I to VII represent seven districts of Wuhan city. (b) Close-up view of the study area with exemplary photos of sinkholes in Lujiajie (①), Fenghuo village (②), Qingling village (③), Changhong village (④), Doubu village (⑤), and the Hanyang Lanjiang Road section (⑥). The six karst zones from L1 to L6 are the Tianxingzhou, Bridge Baishazhou, Zhuankou, Junshan, and Hannan zone. (c) Annual (monthly) statistical histogram of karst collapse in Wuhan.

according to the angular distortion concept (Fernández-Torres et al., 2020), integrating subsidence horizontal gradient, InSAR deformation rates, and municipal construction density for quantifying the level of risk posed by land subsidence to existing infrastructures in Wuhan.

## 2. Study area and datasets

### 2.1. Wuhan city area

Wuhan (29°58′N–31°22′N, 113°41′E–115°05′E), the capital of Hubei Province, lies at the intersection between the Jianghan Plain and the hills of southeastern Hubei. It is divided by the Yangtze River and its largest tributary, Han River, into three large districts, Hankou, Hanyang, and Wuchang, with a total area of 8494 km$^2$, 25% of which is covered by water (Fig. 1a).

Geologically, at the end of the Middle Triassic, strong folds and faults were created by the intense compressive stress oriented in a WNW-ESE direction produced by the Indosinian orogeny. Six karst zones with individual length of approximately 35–63 km and width of 0.5–15 km were subsequently formed. They cover a total area of 1091.51 km$^2$, accounting for 12.85% of the total area of Wuhan (Fig. 1b). After the Middle Pleistocene, the bedrock surface of Wuhan began to receive Quaternary deposition, and more than 95% of the area was covered by Quaternary strata, which consisted of various lithologies including gravel, sand (coarse sand, fine sand, and chalk), and clay. The overall thickness of overlying soil varied from 10 m to 60 m (Luo, 2013; Wang et al., 2020).

Notably, some younger terraces on both sides of the Yangtze River (e.g., Baishazhou-Jiangdi (BSZ) zone denoted with a red dashed box in Fig. 1b) show a typical hierarchical structure of the upper soft soil and lower sand (Dual-layered structure), and the thickness (approximately 20–40 m) of the overlying soil is thicker than that of the oldest terraces. In this zone, from 1931 to 2018, thirty-eight sites with up to 102 sinkholes were recorded, 80% of which were caused by anthropogenic activities, and most of them occurred from April to September from 2005 to 2017 (Fig. 1c). Compared with the consolidation-induced land subsidence in soft soil areas, the long-term karst collapse and subsidence in BSZ zone are more uncertain and everlasting, requiring more attention.

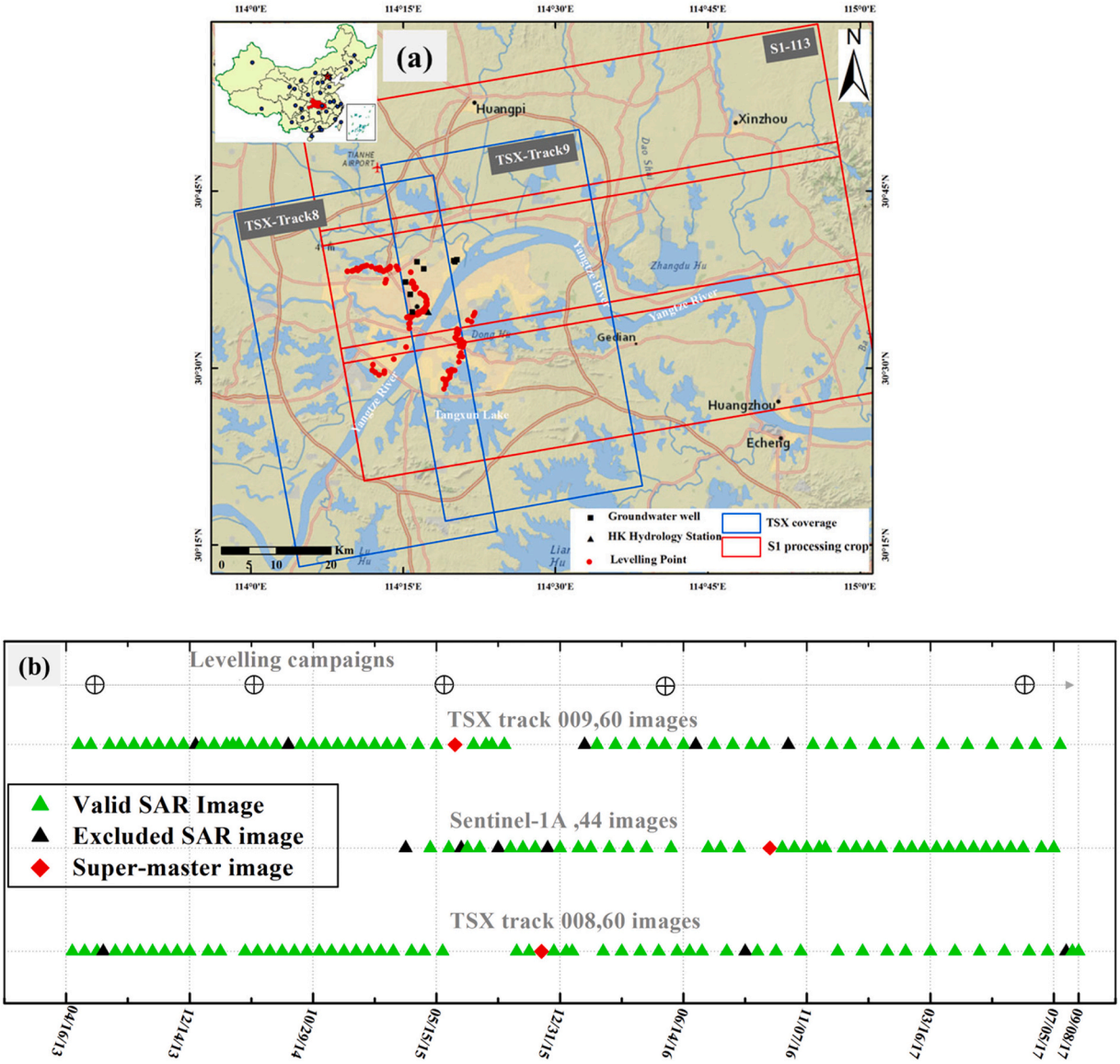


**Fig. 2.** Available datasets. (a) The TerraSAR-X and Sentinel-1A satellite track footprints are shown with blue and red rectangles, respectively. The red solid dots, black squares, and triangles represent the levelling point, groundwater well, and Hankou Hydrological Station, respectively. (b) Temporal distribution of SAR data and levelling campaigns. (For interpretation of the references to colour in this figure legend, the reader is referred to the web version of this article.)

### 2.2. Available datasets

The six karst zones in Wuhan were well imaged by two SAR missions: two tracks of X-band data and one set of C-band data. The first dataset (blue rectangles in Fig. 2a) corresponds to 120 TerraSAR-X (TSX) images acquired from April 2013 to September 2017 along ascending tracks 8 and 9. The second dataset (red rectangles in Fig. 2a) included 44 Sentinel-1A images acquired from an ascending orbit between April 2015 and July 2017. Due to extensive spatial coverage of Sentinel-1A images (250 km wide), only three adjacent bursts of the third swath covering the study area were selected for subsidence analysis in this study.

In situ measurements, including levelling, groundwater, Yangtze River water level, and daily rainfall, were collected for accuracy validation and interpretation of results derived from SAR data. The levelling campaigns consisting of 68 benchmarks along Wuhan metro line 6 and 38 benchmarks along metro line 8, were implemented annually in June by Wuhan Geomatics Institute from 2013 to 2017. The piezometric heads of eight wells were recorded manually or automatically from January 2013 to May 2015. The daily records of Yangtze River water level for Hankou Hydrological Station and Wuhan daily rainfall over the period of SAR images were provided by Changjiang Wuhan Waterway Bureau and National Meteorological Information Centre, respectively. In addition, to provide an in-depth analysis of karst collapse and subsidence in the Baishazhou-Jiangdi zone, we also collected hydrogeological data of this zone, including the stage of karst development, overlying soil structure and thickness, and the spatial distribution of river system, metro lines and large construction sites.

## 3. Methodologies

### 3.1. Interferometric analysis

Small baseline subset processing implemented in StaMPS/MTI (Hooper et al., 2007), was used in this study to derive the spatial and temporal evolution of land deformation using multitrack SAR data. The thresholds of spatial and temporal baselines were 250 m and 90 days for TSX and 200 m and 120 days for Sentinel-1A. Such constraints ultimately yielded 132 and 150 differential interferograms for TSX tracks 8 and 9, analysed using Doris software (Kampes et al., 2003), and 119 differential interferograms for Sentinel-1A data, analysed using GAMMA software (Werner et al., 2000). Subsequently, the selection of slowly-decorrelating filtered phase (SDFP) pixels and time series displacement retrieval were performed in StaMPS/MTI complying with the workflow in Hooper et al. (2007) and Qu et al. (2014). However, some interferograms turned out to be severely contaminated by the long-wavelength phase ramp and short-wavelength turbulence (Bekaert et al., 2015; Haghshenas Haghighi and Motagh, 2019). To achieve satisfactory unwrapping results, we first used a linear fitting to estimate the phase ramp from orbital inaccuracies and the long-wavelength troposphere or ionosphere and then subtracted them from each unwrapped interferogram. For the stratified and turbulent phases, the interferograms were corrected using the atmospheric delay estimated from the Generic Atmospheric Correction Online Service for InSAR (GACOS) (Yu et al., 2018). By testing various grid sizes, 100, 50, and 20 m, for phase unwrapping, we repeated phase estimation and residual unwrapping errors inspection until all interferograms were reliably unwrapped. Finally, the displacement time series and the mean deformation rates were retrieved by least-squares adjustment from these unwrapped small baseline pairs.

### 3.2. Fusion of adjacent-track StaMPS–SBAS results

The mean deformation rates derived from each of the two different tracks are not necessarily similar considering the differences in imaging geometry (incidence angles of tracks 8 and 9 in the overlapping area are approximately 34.6° and 36.6°, respectively), reference point selection, variations in the temporal atmosphere, and distribution of SDFPs (Sun et al., 2017). To homogenize the results, we performed: 1) projecting the line-of-sight results of these two tracks into the vertical direction by dividingcos($\theta$), 2) dividing the overlapping areas into patches with a certain length and width (e.g., 15 m × 15 m in this study) and refining multiple features in each patch into one feature, and 3) aligning the two results based on the mode of differential rates. Finally we obtained the statistics and accuracy of the fusion results as shown in Fig. 3 and Table 1.

As shown from Fig. 3b, the vertical deformation rates difference shows a generalized Gaussian distribution in general, but the mean value is 3.8 mm/yr instead of 0. The mean indicator reflects the overall average, but is severely perturbed by local anomalies. Therefore, it could not be chosen for offset correction of different track results in the Wuhan case. Instead, the mode of vertical deformation rates difference was adopted, i.e., $Mode = 2.5$. As illustrated in Table 1, the standard deviations obtained by the direct differentiation, mean-correction, and mode-correction schemes are 4.2, 3.4, and 2.6 mm/yr, respectively. These results prove the rationality of the mode selection in the fusion approach. Ultimately, we selected track 9 as the reference track and then added the offset to track 8 to calculate the mean deformation rates in Wuhan (Fig. 4).

### 3.3. Soft soil consolidation calculation in soft soil areas

The increase in effective stress and dissipation of pore pressure during underground excavation and engineering dewatering may cause persistent soil consolidation subsidence. Therefore, the hyperbolic model (Park and Hong, 2021; Jiang et al., 2021) was used to calculate the final subsidence ($t \to \infty$) at each location from the InSAR-based deformation time series. Subsequently, the consolidation degree of soft soil was retrieved as the ratio between the subsidence at a specified time and the final subsidence based on Terzaghi's one-dimensional consolidation theory (Terzaghi et al., 1996), and it was combined with the metro construction schedule to further explain the subsidence pattern in Hankou.

### 3.4. Cause–effect analysis in karst zones using geographical detector

To quantitatively investigate the spatial relationship between karst subsidence and sinkhole activity (here, it mainly refers to sinkhole formation mechanism) in the Baishazhou-Jiangdi zone, we used spatial variation analysis of geological conditions using Geo-detector developed by Wang et al., 2010. The method basically includes three modules: 1) differentiation and factor detection, 2) interaction detection, and 3) ecological detection. The first two modules are mainly used in detecting the degree (q-value) to which individual or multiple factors $X_i$ contribute to the attribute variable $Y$.

$$q = 1 - \frac{\sum_{h=1}^{L} N_n \sigma_h^2}{N\sigma^2} \tag{1}$$

where $h = 1, \cdots, L$ represents the categories of attribute variable $Y$ and factors $X_i$; $N_h$ and $N$ are the number of units of the $h$-th and whole strata with variances of ${\sigma_h}^2$ and $\sigma^2$, respectively.

The third module is used in comparing the differences in explanatory importance among different factors for an attribute variable. Given the characteristics of land subsidence and karst collapse in the Baishazhou-Jiangdi zone and the diversity of available data in this zone, we constructed a Geo-detector model, in which the stage of karst development ($X_1$), overlying soil structure ($X_2$) and thickness ($X_3$), proximity to major rivers ($X_4$), abundance in sediment pore water ($X_5$), and proximity to metro lines and construction sites ($X_6$) were factor layers, while the land deformation rate was considered as the attribute$Y$. The aim was to

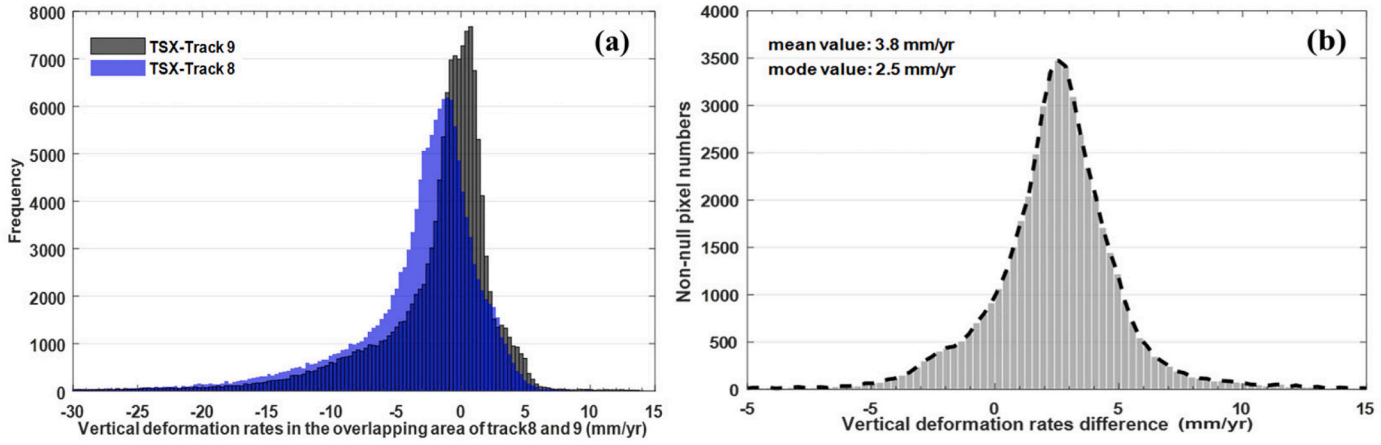


**Fig. 3.** (a) Vertical deformation rates histograms in the overlapping area of TSX tracks 8 and 9. (b) Histograms of the difference in annual vertical deformation rates.

**Table 1**
Results of statistical analysis for the mean and mode-based fusion schemes in the overlapping area.

| Fusion scheme | Mean value (mm/yr) | Minimum (mm/yr) | Maximum (mm/yr) | Standard deviation (mm/yr) |
|---|---|---|---|---|
| Direct differentiation | 3.8 | −36 | 69 | 4.2 |
| Mean-correction | 2.4 | −35 | 66 | 3.4 |
| Mode-correction | 1.1 | −30 | 54 | 2.6 |

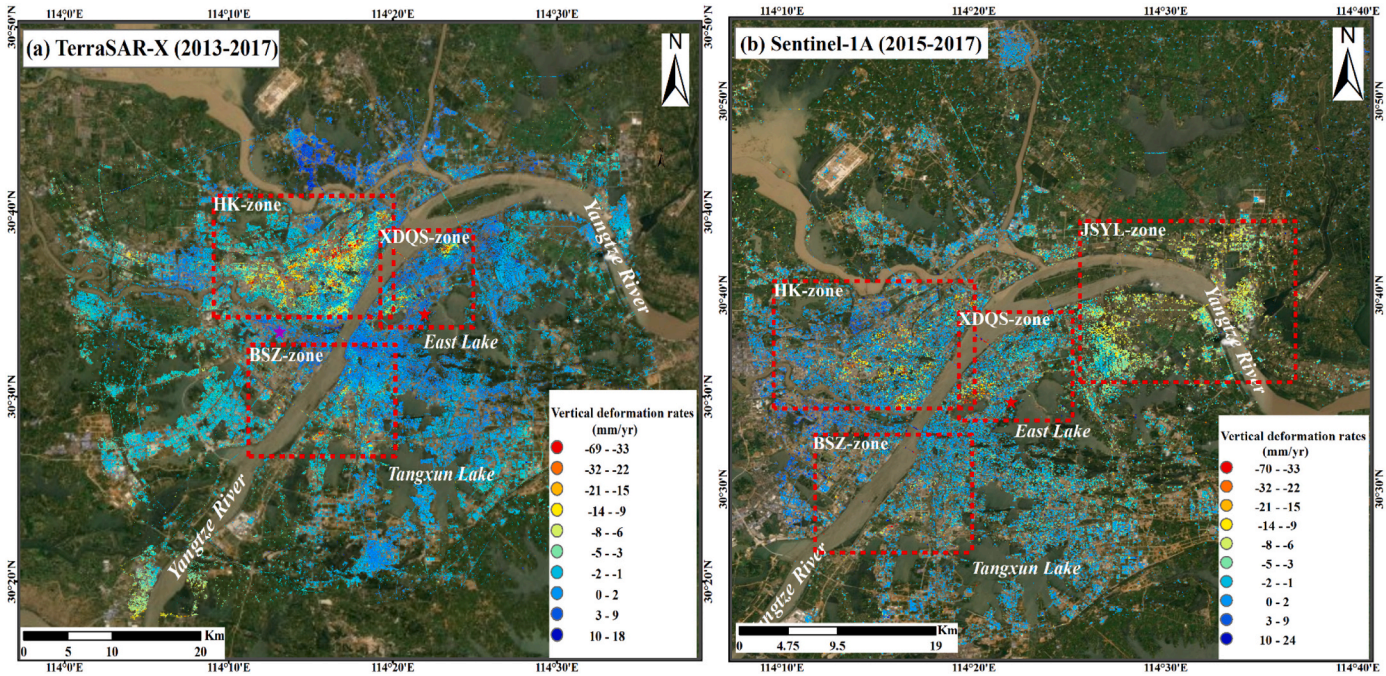


**Fig. 4.** Vertical deformation rates in Wuhan in (a) 2013–2017 and (b) 2015–2017. Positive values (dark blue) represent uplift, and negative values (warm colors) represent subsidence. The purple and red solid stars are used as reference points for tracks 8 and 9, respectively. The red dashed polygons indicate the four major subsidence zones in Wuhan: Hankou (HK-zone), Xudong-Qingshan (XDQS-zone), Baishazhou-Jiangdi (BSZ-zone), and Jianshe-Yangluo zone (JSYL-zone). (For interpretation of the references to colour in this figure legend, the reader is referred to the web version of this article.)

quantitatively detect the q-value and significance between karst subsidence and these nature and human-induced factors.

### 3.5. Land subsidence risk zoning using weighted risk assessment method

Angular distortion is a promising approach for evaluating civil infrastructure damage caused by land subsidence (Skempton and Macdonald, 1956; Cigna and Tapete, 2021). Here, we performed risk assessment of land subsidence in Wuhan according to the angular distortion, which was calculated as the ratio of the subsidence horizontal gradient (*SHG*) between two adjacent pixels to the horizontal distance between them with a slope algorithm available in ArcGIS® software. Given that high *SHG* value implies high shear stress and consequent damage to structures, we set the weight of *SHG* to be three times that of land subsidence rates ($V_{stub}$) (Fernández-Torres et al., 2020). The TerraSAR-X and Sentinel-1A results (Fig. 4) showed that land subsidence

in Wuhan destroyed infrastructures, such as metro line 3 (Fig. 5). To assess the risk to important infrastructures, we exploited municipal construction density (metro lines and large construction sites with building height of over 250 m) ($MC_{den}$) and constructed a risk map as:

$$Risk = ((3 \times SHG) + V_{sub}) \times MC_{den} \quad (2)$$

## 4. Results

### 4.1. Subsidence zones in Wuhan

A high-resolution deformation rates map of Wuhan was obtained through multitemporal and multitrack InSAR processing (Fig. 4a, b). A total of 853,778 and 508,774 SDFPs were extracted through StaMPS-SBAS analysis, and average densities of approximately 332 and 104 SDFPs/km$^2$ were obtained through TSX and Sentinel-1A processing, respectively. As shown in Fig. 4a,b, most of the areas of Wuhan city were relatively stable, but four major subsidence zones were observed (red dashed boxes in Fig. 4a, b), namely, Hankou, Xudong-Qingshan, and Baishazhou-Jiangdi, and Jianshe-Yangluo zone. The first three zones were clearly identifiable in the TSX-based results and to some extent in the Sentinel-1A results due to the low density of SDFPs. The Jianshe-Yangluo zone was located outside the central city of Wuhan (Fig. 4b), and was detected mainly in the Sentinel-1A data due to their large spatial coverage and high level of coherence in differential interferograms.

#### 4.1.1. Hankou and Xudong-Qingshan subsidence zone

Among the four subsidence zones detected in Wuhan, Houhu area in Hankou zone had the largest subsidence, with a maximum rate of approximately −70 mm/yr for both TSX and Sentinel-1A (Fig. 5a). Changfeng area and Xinrong area were two other areas with relatively severe localized land subsidence. The TSX deformation analysis of a profile connecting the three areas showed three phases of deformation in Hankou during the observation period (Fig. 5b). The three phases corresponded to rapid subsidence from April 2013 to May 2015, relative

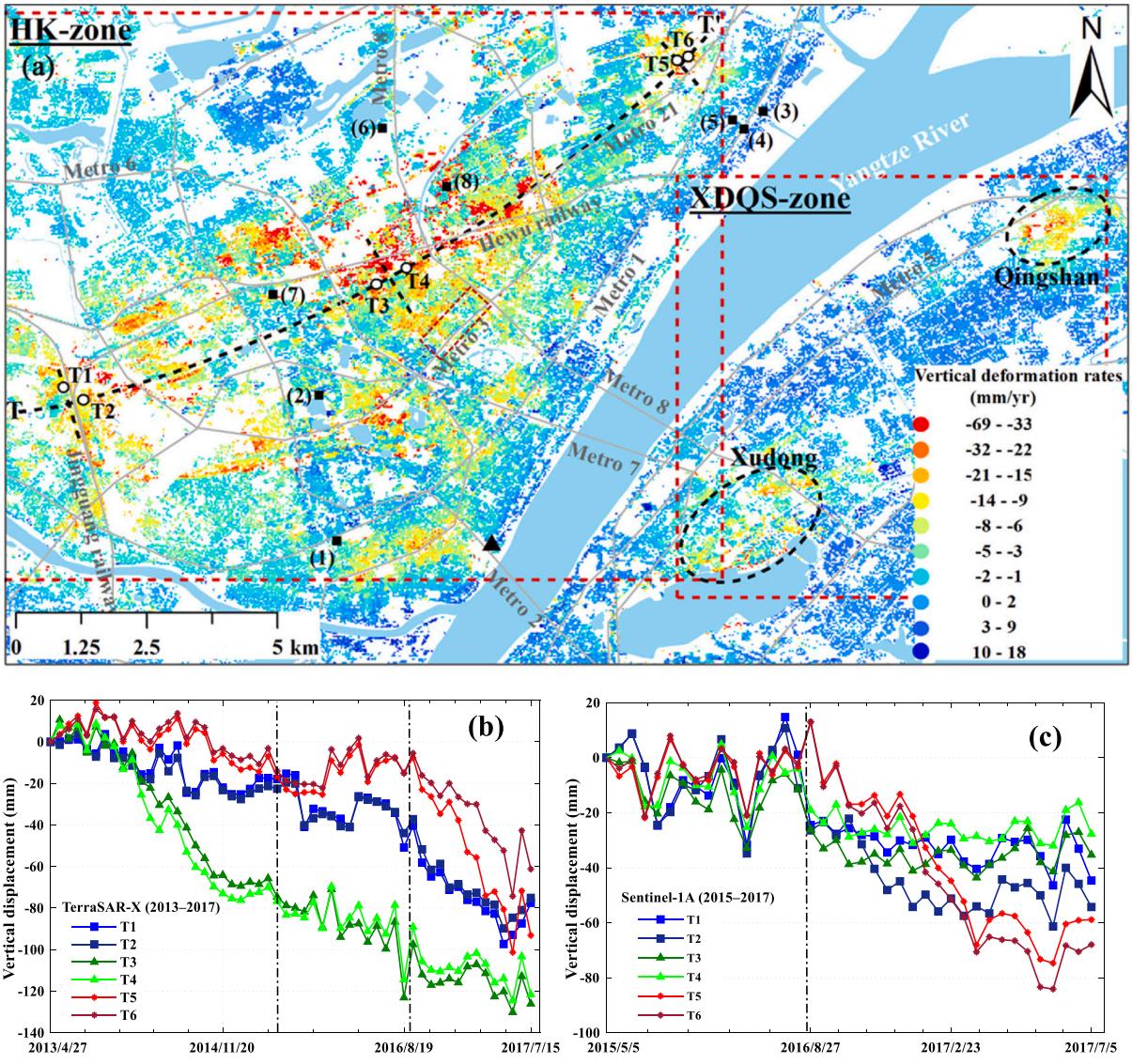


**Fig. 5.** (a) Close-up view of land subsidence rates in Hankou and Xudong-Qingshan zones. Black squares marked with (1)–(8) are groundwater wells. The purple rectangle represents an area of gushing water and sand in the Huiji Road–Hong Kong Road Station section. Grey lines represent the metro under construction: metro 3 (March 2012 to December 2015), metro 6 (November 2013 to December 2016), metro 7 (December 2013 to October 2018), metro 8 (December 2013 to December 2017), and metro 21 (April 2015 to December 2017). (b–c) Displacement time series of six points located in Changfeng (e.g., T1, T2), Houhu (e.g., T3, T4) and Xinrong (e.g., T5, T6). The black vertical dashed lines represent two important time nodes: May 2015 and August 2016. (For interpretation of the references to colour in this figure legend, the reader is referred to the web version of this article.)

stability or low subsidence from May 2015 to August 2016, and accelerated subsidence from August 2016 to July 2017. The nonlinearity in the last two phases of subsidence in Hankou was also clearly observable in Sentinel-1A (Fig. 5c).

In the first phase of subsidence in Hankou zone, a pair of points within each area (e.g., T1/T2 in Changfeng, T3/T4 in Houhu, and T5/T6 in Xinromng) showed the same subsidence trend but with varying degrees of subsidence rates. Houhu appeared to be the most severe area with approximately −40 mm/yr, followed by Changfeng (approximately −10 mm/yr) and Xinrong (approximately −7 mm/yr). In the second phase, the TSX and Sentinel-1A results indicated that the ground was relatively sTable In the third phase, however, the pattern of subsidence characteristics was opposite that of the first phase. Xinrong became the most severe subsidence area with rates higher than −51 mm/yr according to TSX and − 57 mm/yr according to Sentinel-1A, followed by Changfeng (approximately −25 mm/yr by TSX and − 30 mm/yr by Sentinel-1A) and Houhu (approximately −7 mm/yr by TSX and − 9 mm/yr by Sentinel-1A). Note that several other clusters of subsidence were also evident, most of which were located along metro lines 3, 6, and 7 (Fig. 5a).

Similarly, the Xudong-Qingshan zone, located in the heavy industrial and dense municipal construction area on the east bank of the Yangtze River, had two distinct subsidence funnels with maximum rates reaching −34 mm/yr (Qingshan) and − 31 mm/yr (Xudong) according to the TSX results (Fig. 5a). The location and deformation degree of the subsidence funnels were consistent with those of a previous study that used Sentinel-1A images from 2015 to 2017 (Han et al., 2020). The extended SAR processing results after 2017 showed that the two subsidence funnel tended to expand and connect, although their subsidence rates decreased to approximately −11 mm/yr (Han et al., 2020; Jiang et al.,

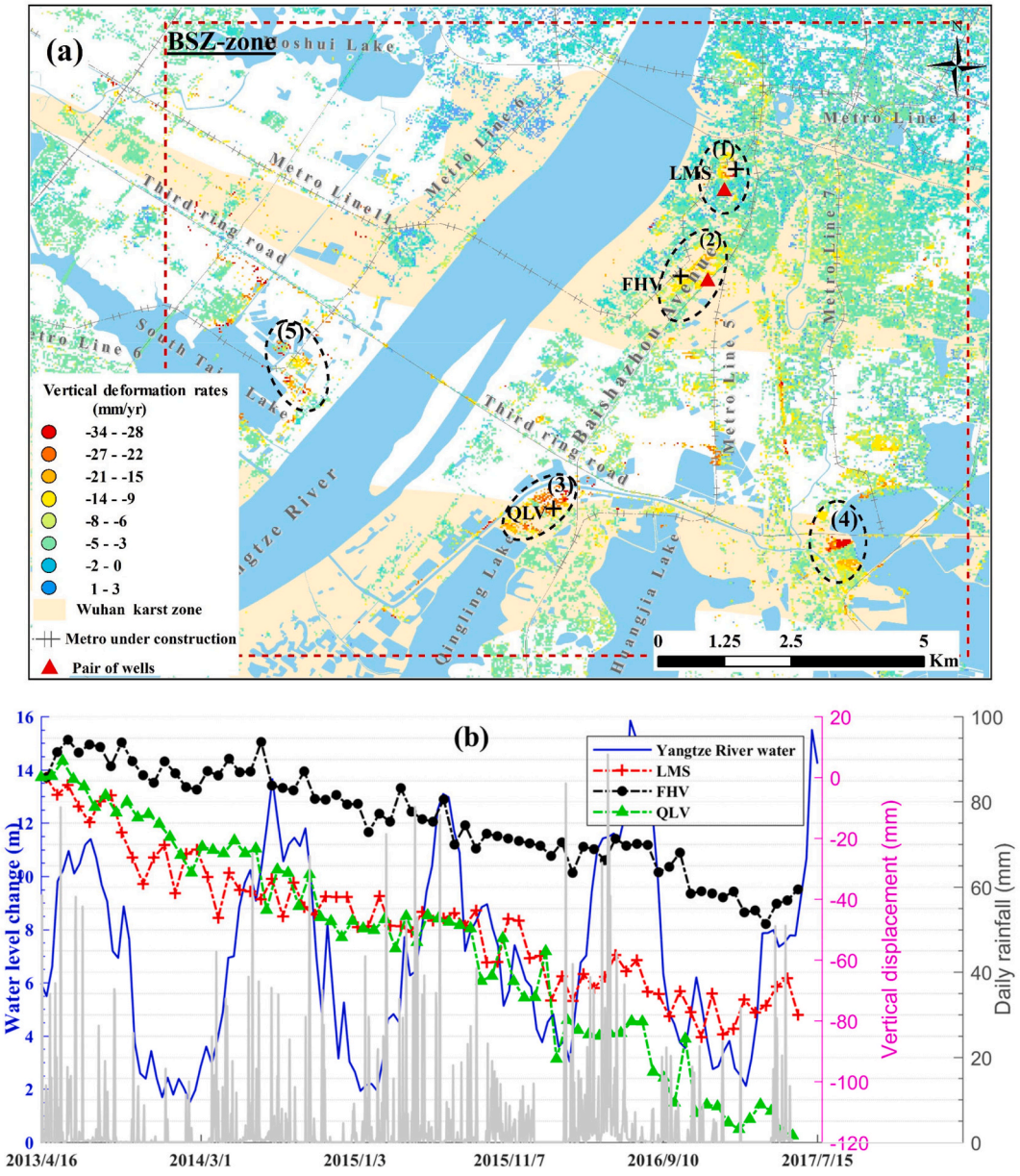


**Fig. 6.** (a) Close-up view of land subsidence rates based on TSX in the Baishazhou-Jiangdi zone in the L3 and L4 karst zones. (1) Lujiajie (LMS); (2) Fenghuo village (FHV); (3) Qingling village (QLV); (4) Hongqiao community and (5) Jiangxu industrial park. Red triangles indicate the boreholes used to monitor shallow groundwater and karst water levels. The three black crosses, LMS, FHV and QLV, located in (1), (2) and (3), respectively, indicate areas with a high number of sinkhole incidents and ongoing land subsidence in Wuhan. (b) Time series of the Yangtze River water level and displacement evolution at LMS, FHV, and QLV based on TSX results. (For interpretation of the references to colour in this figure legend, the reader is referred to the web version of this article.)

2021).

#### 4.1.2. Baishazhou-Jiangdi subsidence zone

Fig. 6a shows the land deformation rate results of TSX in the Baishazhou-Jiangdi zone. The most severe subsidence areas were located in the Hongqiao community (4) and Jiangxu industrial park (5), which had maximum subsidence rates of −34 and − 32 mm/yr, respectively. In addition, some sites, such as Lujiajie (1), Fenghuo village (2), and Qingling village (3), had the largest concentrations of historical karst collapse sites (e.g., denoted with ①, ②, and ③ in Fig. 1b), which were currently undergoing severe land subsidence (Fig. 6a, b). The mentioned five subsidence areas were basically located in the L3 and L4 karst zones (Fig. 1b), and some metro lines under construction, such as metro lines 7, 6, 5, and 11, passed through them.

#### 4.1.3. Jianshe-Yangluo subsidence zone

The Jianshe-Yangluo zone is located in the outlying suburbs of Wuhan and extends beyond the eastern boundary of the TerraSAR-X frame, where the X-band SAR data suffer from more severe decorrelation than the C-band SAR data. Therefore, the deformation results based on Sentinel-1A were mainly represented in this zone (Fig. 7a). The Wuhan Iron and Steel Company (WISC), Sinopec Wuhan Company (SWC), Huaneng Yangluo Power Plant (HYPP), and Yangluo Cement Plant (YCP) were located there and exhibited maximum rates of −17, −12, −30, and − 23 mm/yr, respectively (Fig. 7a). The uneven land subsidence of these heavy industrial clusters had resulted in the fracturing of the surrounding housing and pavement, for example, a 2–3 cm crack was found in a building near the YCP and HYPP subsidence areas, and pavement cracks appeared near the WISC (Fig. 7b, c).

Since 2016, the Yangluo Economic Development Zone (YLDZ), integrating industrial clusters, port logistics, and living services, has been under full-scale construction, which has led to the rapid formation of a new subsidence zone with a prevailing rate of −21 mm/yr (Fig. 7a). Fig. 7d presents the deformation time series for three construction sites located in the YLDZ. The displacement time series at these sites revealed accelerated land subsidence (from the previous −9 mm/yr to −19 m/yr) that occurred after January 2016, when large-scale construction commenced.

### 4.2. Accuracy and consistency assessment

An accuracy assessment of the InSAR-derived deformation results was performed by comparing them with the precise levelling measurements (Fig. 8a). All SDFPs falling within a circle radius of 50 m cantered on a levelling point were processed as one and compared with the deformation rate of the levelling point. We took TSX as an example due to its high resolution and because it almost had the same time span as the levelling campaign. The overall RMSE was 2.5 mm/yr, the minimum difference was 0 mm/yr, and the maximum was 9 mm/yr. The linear regressions suggested that the coefficient of determination ($R^2$) between InSAR and levelling-based deformation rates was 0.79. To assess the consistency of different SAR sensors, we compared the results from TSX and Sentinel-1A. The central district of Wuhan, comprising the main subsidence zones (e.g., Hankou, Xudong-Qingshan, and Baishazhou-Jiangdi), were chosen for the analytical samples. The mean vertical deformation rates from TSX and Sentinel-1A were resampled to a uniform 90 m grid and then compared through linear regression analysis. The correlation is demonstrated in Fig. 8b, showing the RMSE and $R^2$ value: 3 mm/yr and 0.63, respectively. Comparisons in Fig. 8a and Fig. 8b indicated the high accuracy and overall consistency of these two

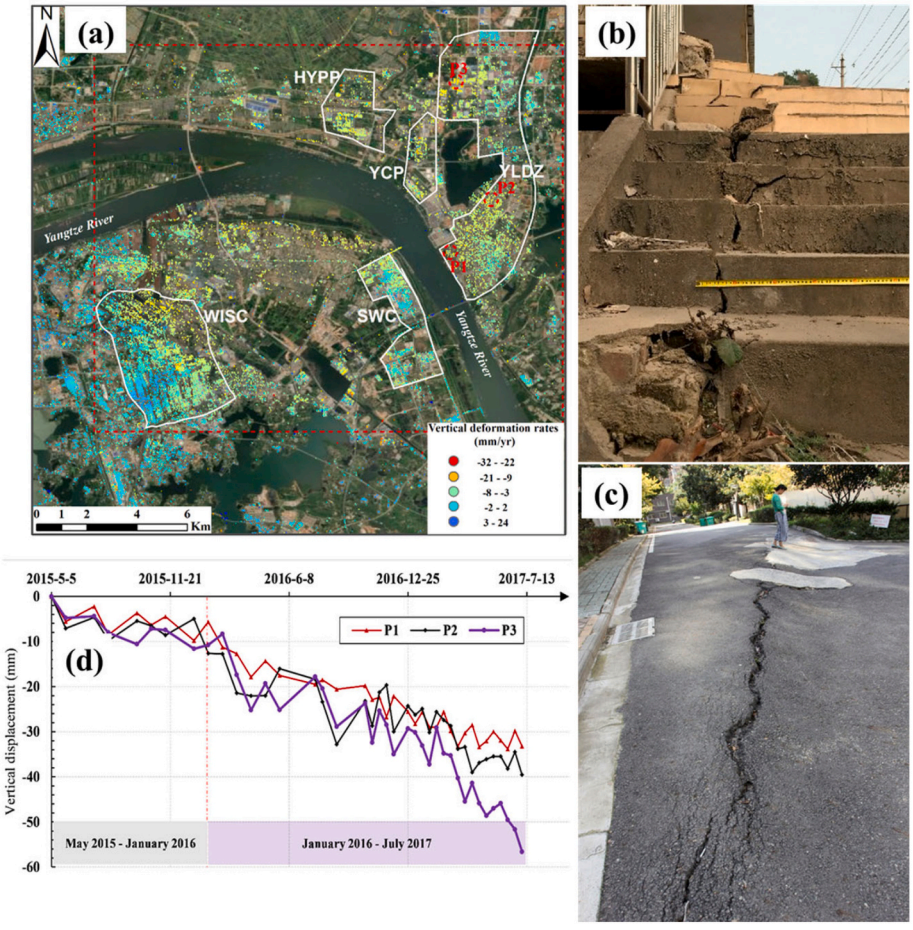


**Fig. 7.** (a) The 2015–2017 mean deformation rates based on Sentinel-1A in the Jianshe-Yangluo zone. White solid polygons represent four heavy industrial clusters: Wuhan Iron and Steel Company (WISC), Sinopec Wuhan Company (SWC), Huaneng Yangluo Power Plant (HYPP), and Yangluo Cement Plant (YCP), and the Yangluo Economic Development Zone (YLDZ). (b–c) Examples of structure and pavement damage caused by uneven subsidence provided by Zhou et al., 2017. (d) Displacement time series corresponding to areas P1, P2, and P3 in Fig. 7a. The red vertical dashed line represents the ninth image of Sentinel-1A on January 24, 2016. (For interpretation of the references to colour in this figure legend, the reader is referred to the web version of this article.)

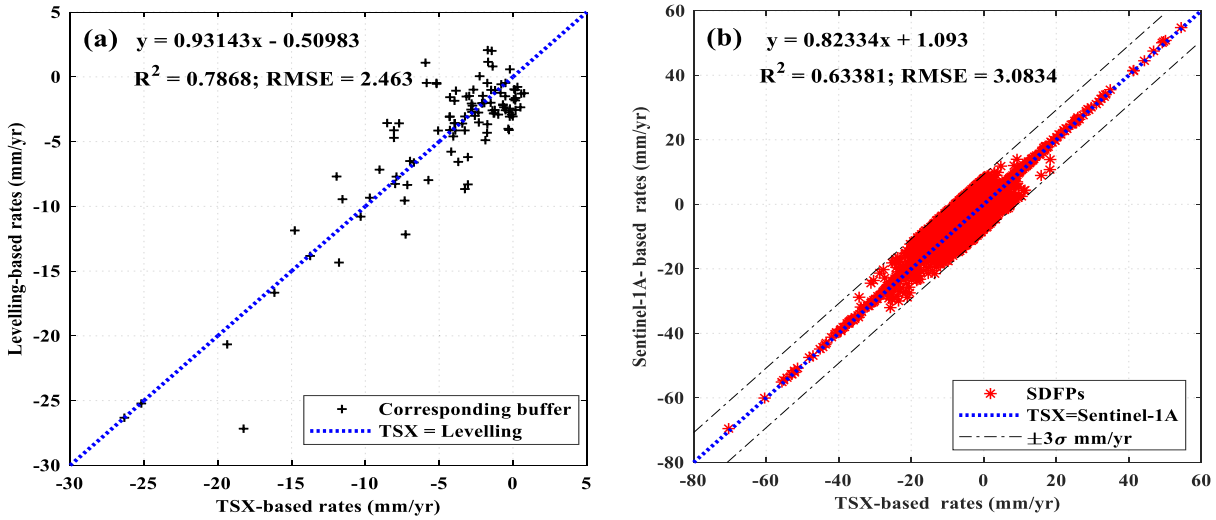


**Fig. 8.** (a) Regression between the mean vertical deformation rates of TSX and the linear levelling deformation rates. (b) Correlation between the deformation rates derived from TSX and Sentinel-1A within the central district of Wuhan. The two sets of results were resampled to a grid of 90 m × 90 m.

sets of InSAR results.

### 4.3. Governing factors of karst subsidence

Fig. 9b–g show the grading of potential influencing factors in the Baishazhou-Jiangdi zone. The q-values of the influencing factors with respect to karst subsidence in the Baishazhou-Jiangdi zone (Fig. 9a) were subsequently extracted using Geo-detector (Table 2). The principal diagonal of Table 2 shows the q-value, and elements below and above the principal diagonal represent the combined effects of multiple factors on karst subsidence and their importance, respectively. The stage of karst development was the most important factor affecting the spatial distribution of karst subsidence (0.0599), followed by proximity to metro lines and construction sites (0.0450), proximity to major rivers (0.0364), overlying soil structure (0.0339), abundance in sediment pore water (0.0305), and overlying soil thickness (0.0179).

### 4.4. Land subsidence risk zoning results in Wuhan

Four categories of angular distortion level were considered in previous studies: low ($\beta \leq 1/3000$), medium ($1/3000 < \beta \leq 1/1500$), high ($1/1500 < \beta \leq 1/500$), and very high ($\beta > 1/500$), indicating an increased likelihood of damage (Skempton and Macdonald, 1956; Cigna and Tapete, 2021). However, as the land deformation rates in Wuhan were generally low, and no grids with the derived *SHG* exceeded 0.002 rad, that is, 1/500, we adopted the natural break algorithm in ArcGIS® to categorize the areas according to their *SHG* values as follows: between 0.0121 and 0.125, as risk level–I; between 0.0033 and 0.0121, as risk level–II; between 0.0015 and 0.0033, as risk level–III, and between 0 and 0.0015, as risk level–IV (Fig. 10a). On this basis, we weighted and superimposed the densities of metro lines and construction sites (Fig. 10b) to finally obtain the risk zoning results in Wuhan, that is, 0.519–1.236 (level–I), 0.0125–0.519 (level–II), 0–0.0125 (level–III), and − 0.0838–0 (level–IV) (Fig. 10c).

## 5. Discussion

The spatial analysis of land subsidence in Wuhan with high-resolution X-band and moderate resolution C-band radar satellites revealed that the subsidence zones were generally located in urbanized or industrialized clusters and areas with well-developed karst, which were distributed on both sides of the Yangtze River.

### 5.1. Land subsidence in soft soil areas

Fig. 11 shows the structure and thickness of the Quaternary soil layer in Wuhan. The Hankou, Xudong-Qingshan, and Jianshe-Yangluo zones are mainly distributed on the younger terraces on both sides of the Yangtze River and are composed of compressible soft soil that varies in thickness from 10 m to 50 m.

As with other studies (Bai et al., 2017; Zhou et al., 2017; Han et al., 2020; Jiang et al., 2021), we identified Hankou district as the most extensive and locally affected subsidence zone (e.g., Houhu area). Historically, the Houhu area mainly consisted of paddy fields and lakeshores, and the upper surface generally consisted of silty soil with low bearing capacity and high compressibility. In modern times, owing to the filling and reclamation of the lake, muddy soft soil has formed on the exposed surfaces of the artificially filled lakes and marshes, thus creating an engineering geological environment with high compressibility and rheology (Wang et al., 2007). In this soft soil geological environment, groundwater changes can directly trigger land deformation (Motagh et al., 2008, 2017; Zhu et al., 2015; Haghshenas Haghighi and Motagh, 2019; Cigna and Tapete, 2021). To better quantify this relationship, we collected water level data from eight groundwater wells (see the black squares labelled (1)–(8) in Fig. 5a) located near different metro lines.

The wells labelled (1)–(5) are automatic monitoring wells, and those labelled (6)–(8) are manual monitoring wells. As shown in Fig. 12, complete observational data for two years were available for most wells. The Jianzhu (7) and Tazihu (8) wells in the Houhu subsidence area and northern Houhu area showed strong correlations between decline in water level and vertical subsidence. For instance, the TSX-based results showed that from April 2013 to December 2014, the land subsided by 45 mm, and groundwater decreased by 6.2 m at the site of Jianzhu. Similarly, 56 mm of land subsidence and 4.2 m of groundwater decline were observed in the Tazihu site (Fig. 12). Groundwater levels in the areas of Tianyi, Wanjing, Baibuting-3 and Menghu ((1), (2), (5), (6) in Fig. 12) fluctuated moderately, with mean water level changes of −1.43, 0.9, −0.67 and − 0.48 m, respectively. From Fig. 12, the land surface was relatively stable around these wells, with a cumulative deformation of 2.2, 1.9, −3.8, and 2.5 mm during the groundwater level-monitoring period (Fig. 5a and Fig. 12). Although the magnitudes of groundwater level declines and land subsidence at the four well sites were relatively small, synchronous characteristics were observed because the overall correlations of the two sequences at each well site were 0.49, 0.46, 0.15, and 0.58. In addition, Fig. 12 shows that the displacement time series and groundwater change were not obviously correlated with the change

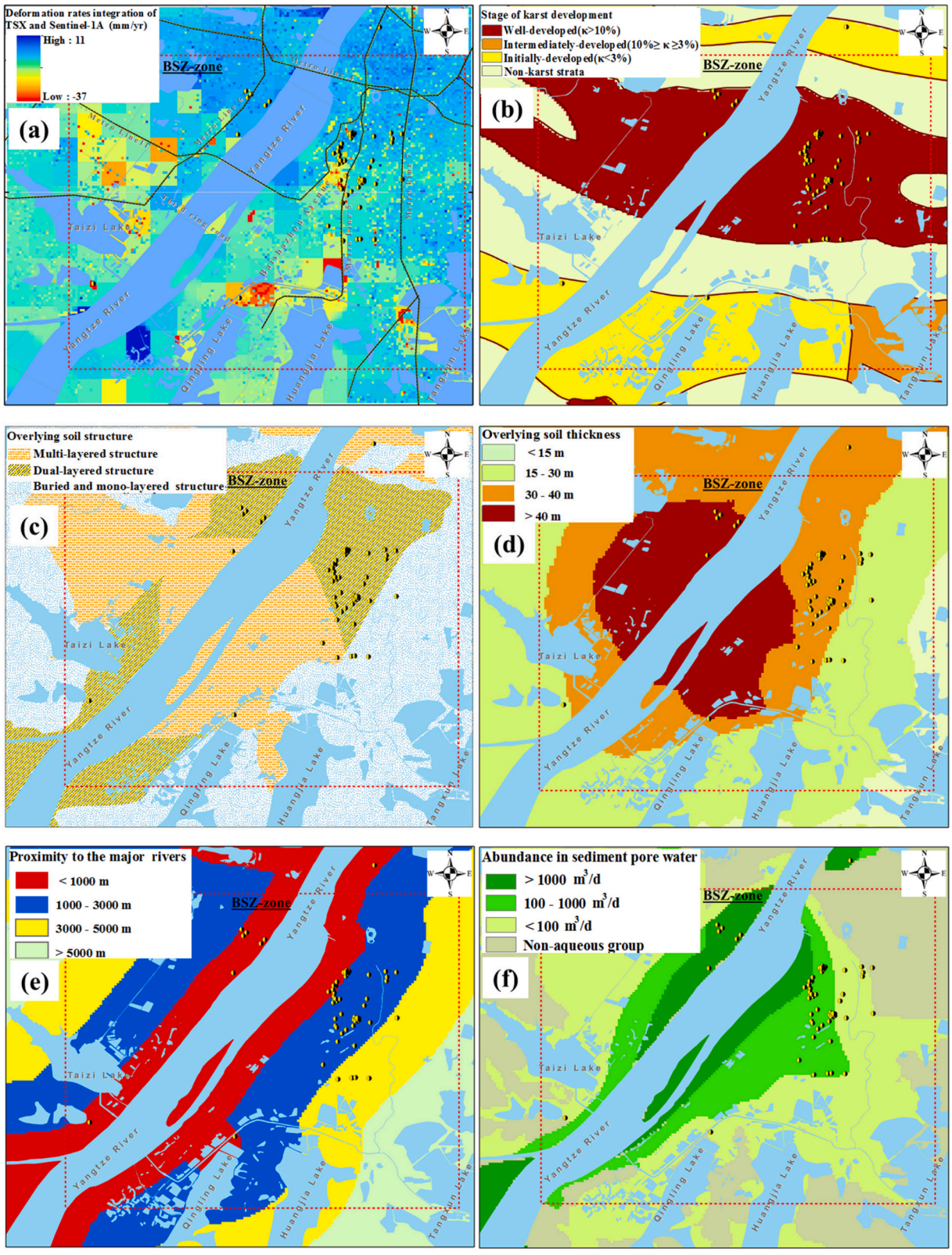


**Fig. 9.** Potential subsidence-induced factors and subclasses. (a) InSAR-based land deformation rates in Baishazhou-Jiangdi zone; (b) stage of karst development; (c) overlying soil structure and (d) thickness; (e) proximity to the major rivers; (f) abundance in sediment pore water; (g) proximity to metro lines and construction sites with a building height of over 250 m.

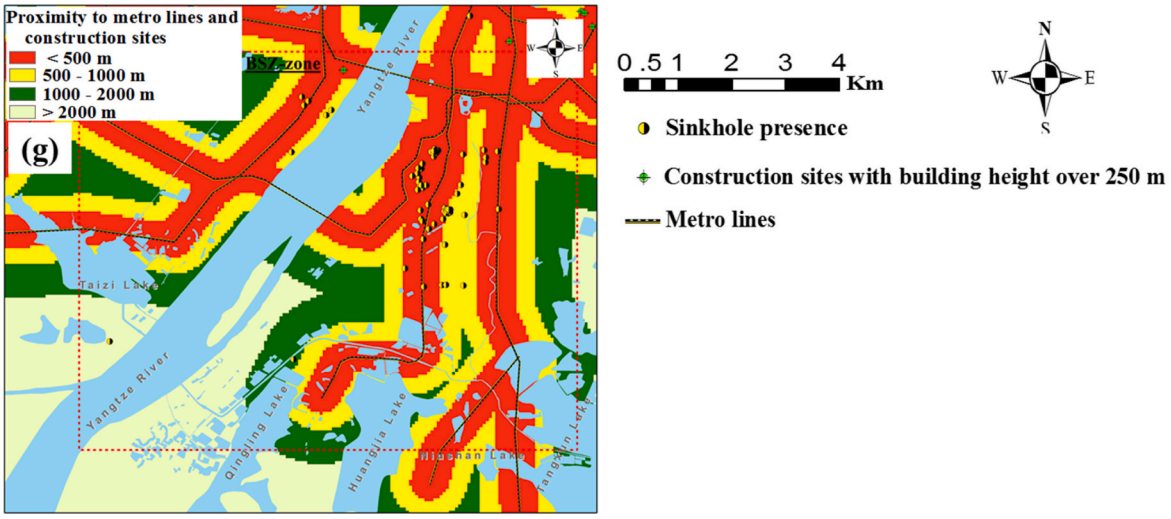


**Fig. 9.** (*continued*).

**Table 2**
Results of the subsidence-induced factor differentiation, interaction and ecological detection. The principal diagonal values represent the q-value of the single factor. Abbreviation "Y" or "N" express the statistically significant differences between two environmental risk factors.

| Factors | Stage of karst development ($X_1$) | Overlying soil structure ($X_2$) | Overlying soil thickness ($X_3$) | Proximity to major rivers ($X_4$) | Abundance in sediment pore water ($X_5$) | Proximity to metro lines and construction sites ($X_6$) |
|---|---|---|---|---|---|---|
| $X_1$ | 0.0599 | N | Y | N | Y | N |
| $X_2$ | 0.0818 | 0.0339 | N | N | N | N |
| $X_3$ | 0.0662 | 0.0705 | 0.0179 | N | N | Y |
| $X_4$ | 0.1263 | 0.0977 | 0.0936 | 0.0364 | N | N |
| $X_5$ | 0.1081 | 0.0519 | 0.0456 | 0.0936 | 0.0305 | N |
| $X_6$ | 0.1640 | 0.0824 | 0.0519 | 0.0713 | 0.1233 | 0.0450 |

in Yangtze River water level in the two most severe subsidence areas: Jianzhu (7) and Tazihu (8), revealing that the influences of natural factors on land subsidence were not dominated in this non-karstic soft soil areas. Therefore, groundwater depletion in soft soil areas was the main driver of ground subsidence.

It is worth noting that groundwater extraction has been restricted in Wuhan since 2013. However, 47 skyscrapers of over 250 m in height (https://www.163.com/dy/article/FTSV7SQ90534FOQ8.html) and five metro lines (e.g., metro lines 3, 6, 7, 8, and 21 in Fig. 5a) were under construction in Hankou district during the InSAR observation period of this study. Many of these under-construction sites and metro lines were concentrated in the Houhu area, such as the Tazihu Sports Centre and metro lines 6, 8, and 21. The engineering dewatering process resulting from intensive surface pit construction and underground excavation inevitability affected the groundwater levels of the six wells mentioned above and thus reduced pore aquifer pressure, which in turn led to land deformation.

In addition, the temporal characteristics of subsidence revealed by InSAR time series analysis indicated that the rate of compaction in Hankou was not constant and varied over time (Fig. 5b, c). To better investigate the reason for this nonlinearity, we used the InSAR subsidence time series of the three subsidence centres (T2, T4, and T6 in Fig. 5b, c) and calculated the degree of soft soil consolidation at the corresponding time nodes (Table 3).

From Table 3, the average degrees of soft soil consolidation in the Changfeng (T2), Houhu (T4), and Xinrong (T6) areas between April 2013 and May 2015 were 28.53%, 33.67%, and 12.57%, respectively. During these periods, the initial intense construction of metro lines 3, 6, and 8 and the Wuhan Science and Technology Innovation Park project resulted in land subsidence of −10, −40, and − 7 mm/yr in the first phase at these three locations. After rapid consolidation soft soil in the first phase, the degree of soft soil consolidation at the T2, T4, and T6 sites increased slightly from May 2015 to August 2016 (maximum increase of 13% for T2). This increase can be attributed to the suspension of construction and the completion of the metro section. For example, on February 10, 2015, the gushing of water and sand in the shield section between Huiji Road and Hong Kong Road Station (see the purple dashed rectangle in Fig. 5a) on metro line 3 presented risk, and thus the project was stopped for maintenance. Land subsidence was halted during this time. In May 2015, the excavation construction for metro line 6 was completed, and pavement laying began. In December 2015, metro line 3 was completed. It is worth noting that after August 2016, the rates of soft soil consolidation considerably increased, especially at the Changfeng (T2) and Xinrong (T6) sites, increasing to 34% and 60%, respectively, in just one year (August 2016–July 2017); These increases caused ground subsiding of −25 and − 51 mm/yr at these two sites, respectively. During this period, the construction of metro line 21 started from Houhu via Xinrong area. Moreover, metro lines 6 and 3 were put into operation one after another. The combined effects of the underground excavation interference of metro line 8 and the long-duration cyclic vibration load of the operating metro lines weakened the soil's dynamic stability and pore aquifer pressure (Ge et al., 2008), thus accelerating land subsidence.

The Xudong-Qingshan zone had a subsidence pattern similar to that of Houhu area, and the under-construction metro lines 5, 7, and 8 passed through the zone (Fig. 5a). The under-construction Greenland Centre, which was Wuhan's tallest building, and Wuhan Iron and Steel Works, which was Wuhan's oldest heavy industry, were also located in this zone (Fig. 7a). Most of the areas of the Jianshe-Yangluo zone were located in the multi-layered structure soft soil area, with an overlying soft soil thickness of 40 m (Fig. 11). In general, soft soil with a thicker multi-layered structure is more likely to subside because shallow groundwater pressure decreases rapidly with excessive engineering dewatering work (Tomás et al., 2010). This situation was observed in the Jianshe-

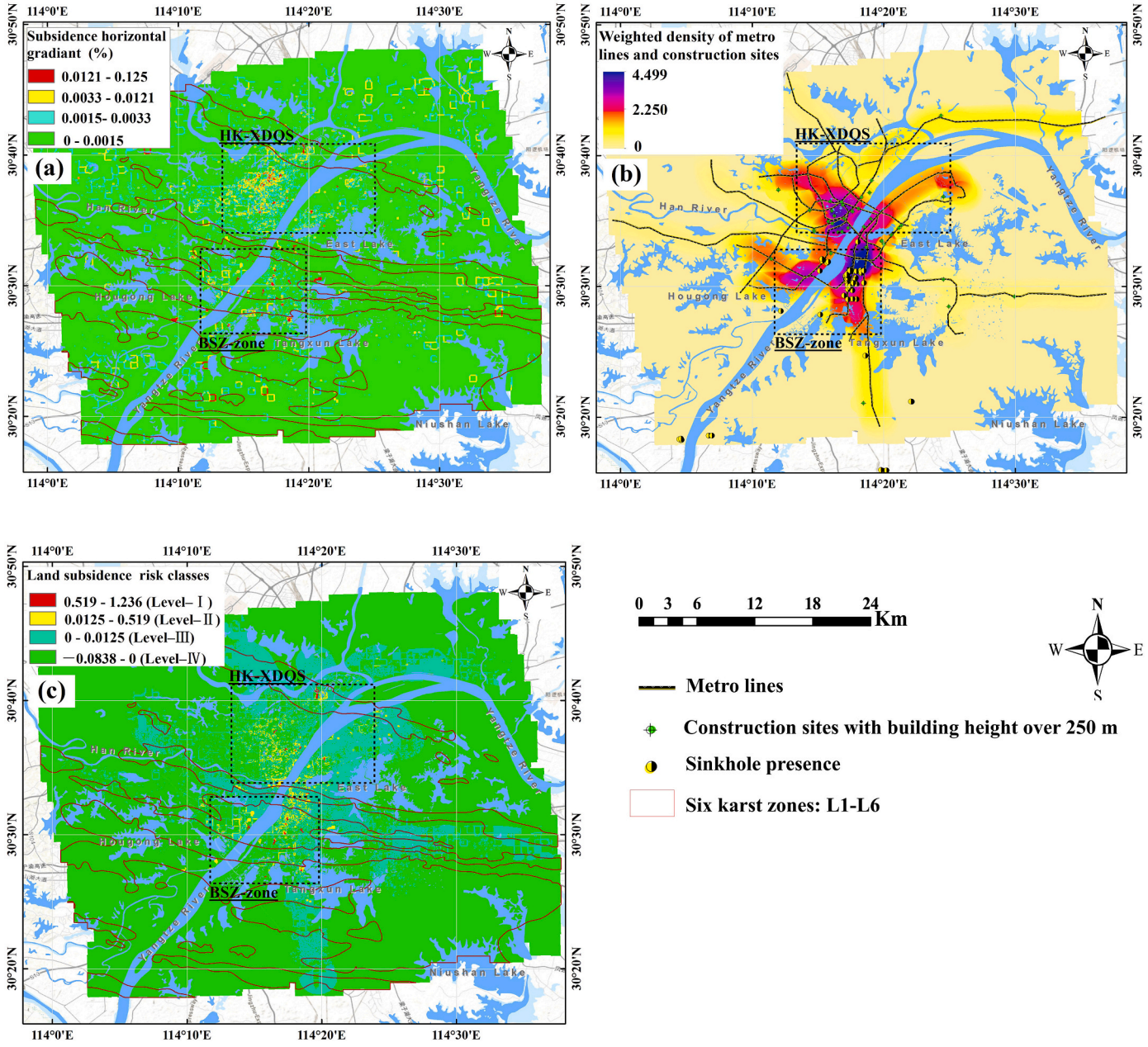


**Fig. 10.** (a) Subsidence horizontal gradient using the integration of TSX and Sentinel-1A-based results in Wuhan; (b) combined weighted density of metro lines and construction sites with building height over 250 m; (c) land subsidence risk zoning maps based on weighted risk assessment.

Yangluo zone. According to the Wuhan Urban Development Plan, the Jianshe-Yangluo zone has undergone large-scale construction since 2016, including "three vertical and six horizontal" main roads, three rail lines, and an international shipping port. By the end of 2020, the scale of urban construction land expanded from the previously planned 35 $km^2$ to 54 $km^2$. The area continued to increase its share of the entire zone's construction land allocation targets (82.6 $km^2$), leading to its rapid evolution into a new subsidence zone in Wuhan.

### 5.2. Land subsidence in karst areas

Approximately 71% of karst collapse incidents in Wuhan occurred in the Baishazhou-Jiangdi zone (Fig. 1b), and in particular, some historical karst collapse sites in this zone are still undergoing severe localized land subsidence, such as Lujiajie, Fenghuo village, and Qingling village ((1), (2), and (3), respectively, in Fig. 6a, b). Compared with land subsidence due to consolidation mechanisms in soft soil areas, the triggers of localized land subsidence in karst areas may be more complex.

#### 5.2.1. Well-developed karst geological conditions

The Baishazhou-Jiangdi zone lies mainly on the first terrace on both sides of the Yangtze River. Loose surface alluvium constitutes a typical hierarchical structure of upper soft soil and lower sand, and the thickness of the upper soft soil generally ranges from 2.7 m to 10.8 m and from 10.6 m to 24.5 m in the lower fine sand (Xu, 2016; Wang et al., 2020). Moreover, three karst zones; Daqiao (L2), Baishazhou (L3), and Zhuankou (L4) traverse this zone (Fig. 6a). Field drilling in this zone revealed that cave encounter rates ranged from 46.0% to 50.1%, and linear karstification rates ranged from 5.9% to 6.0%. Approximately 30% of the detected karst caves were unfilled or semifilled with water (Luo, 2013). This well-developed karst geological condition inevitably provides a channel and storage space for overlying soil materials that are

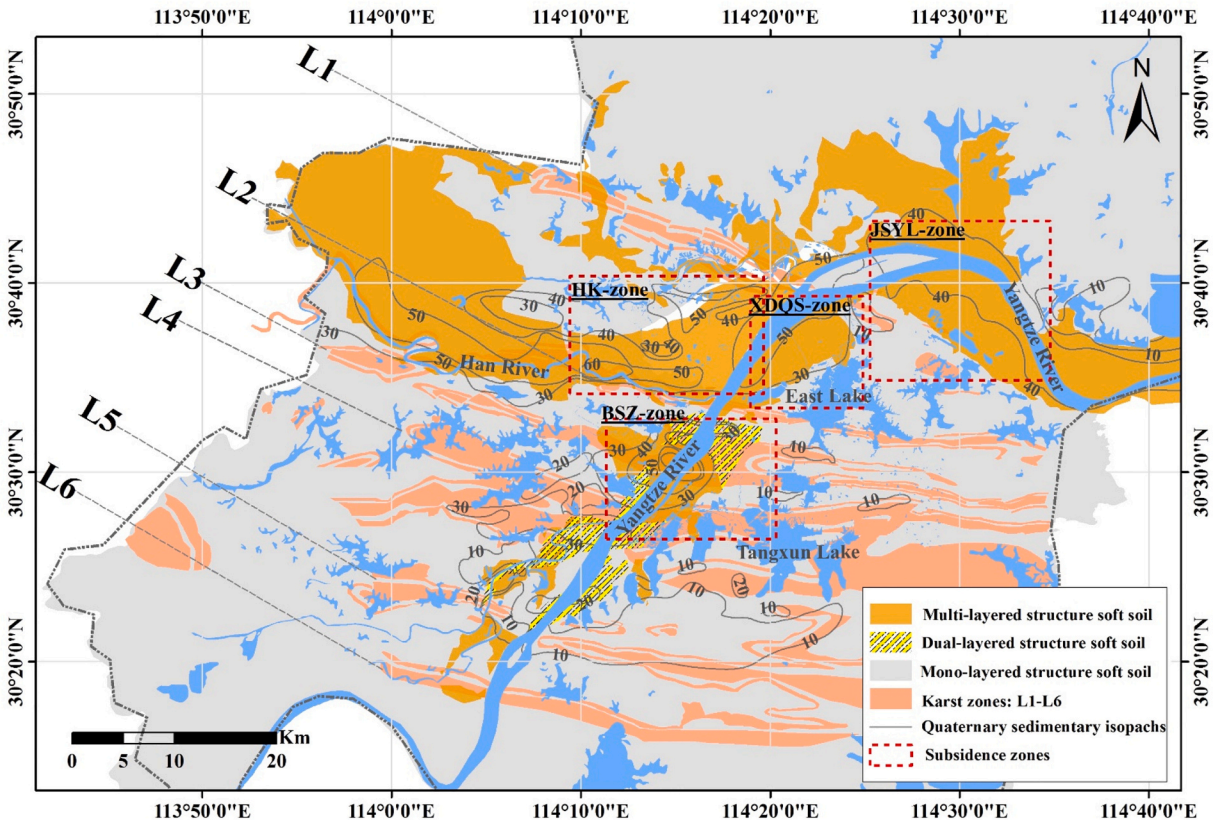


**Fig. 11.** Quaternary sedimentary soil in Wuhan and thickness contours.

transported to caves, promoting the formation of funnel-shaped loose bodies or soil caves and localized land subsidence.

#### 5.2.2. *Connectivity analysis of shallow groundwater, karst, and Yangtze River water*

Wang et al. (2020) suggested that stratigraphic permeability in the Baishazhou-Jiangdi zone gradually increases from shallow to deep and contributes to a special water-bearing system characterized by the vertical flow of the upper groundwater and three-dimensional diffusion of the lower groundwater. Then, to what extent the shallow groundwater, lower and deeper karst water, and the Yangtze River water permeate vertically or runoff laterally?

Regarding the first issue, we obtained groundwater data for two historical karst collapse sites (i.e., Lujiajie Middle School and Fenghuo village, labelled (1) and (2), respectively, in Fig. 6a) from the Hubei Geological and Environmental Centre. Each karst collapse site had two wells, which were approximately 20–30 m apart, and were used to record the daily shallow groundwater and karst water level at the site in 2013. Fig. 13a, b shows the daily groundwater level variation derived from the difference in water levels recorded at 8:00 am between two consecutive days. As shown in Fig. 13, a strong correlation was found between karst water level fluctuations and shallow groundwater changes, and both were generally synchronized with seasonal rainfall. Moreover, the magnitudes of water level variations in these two sequences from June to August 2013 (flood peak periods) were higher than those of the other periods. These results indicate that in this well-developed karst area, rainfall infiltrated and recharged shallow groundwater quickly, and the vertical hydraulic connection between the two water layers was good.

In terms of lateral runoff, we compared the fluctuations in the three types of water levels (Fig. 14). As shown in Fig. 14, the karst water level was lower than the shallow groundwater, but the two generally had synchronous oscillation characteristics. Meanwhile, the shallow groundwater level was lower than the Yangtze River water level during the flood peak period. In other seasons, the shallow groundwater level was higher than the Yangtze River level. However, their overall fluctuation characteristics were consistent, indicating that the lateral runoff of the shallow groundwater was unobstructed and received recharge or was discharged to the Yangtze River in specific seasons. This process influenced the dynamic strength of the soil body, which in turn resulted in karst collapse and subsidence (He et al., 2010).

### 5.3. *Dominant factors contributing to karst subsidence*

The relationship between land subsidence and sinkhole activity is complex and depends on many factors, including hydrogeological conditions and types of sinkholes (Jia et al., 2018; Galve et al., 2015; Shi et al., 2019; Orhan et al., 2021). For example, Orhan et al. (2021) found that sinkhole activity in the Karapınar region in Turkey was limited to areas with low rates of subsidence and attributed this phenomenon to the strong cohesion of the near-surface rock layer that resisted subsidence. Galve et al. (2015) found that ground motion in Ebro Valley was mainly related to continuous long-sustained subsidence activity in large depressions and collapse sinkholes and less frequently to the sudden occurrence of small collapse sinkholes. In Wuhan, we observed that QLV, which had hosted a considerable number of historical sinkhole incidents, also exhibited subsidence rates of −29 mm/yr (Fig. 6a). In the present study, the degree to which driving factors contribute to the land subsidence was explored through Geo-detector analysis (Fig. 9a–g and Table 2). Our findings were consistent with the above multitemporal quantitative or qualitative analysis of individual points, indicating that the well-developed karst conditions play a key role in influencing land subsidence in Wuhan. However, the effects of other factors such as intensive urban construction and proximity to the major rivers were also noticeable. Moreover, we found that the interactions among multiple factors on the spatial distribution of subsidence (below the principal

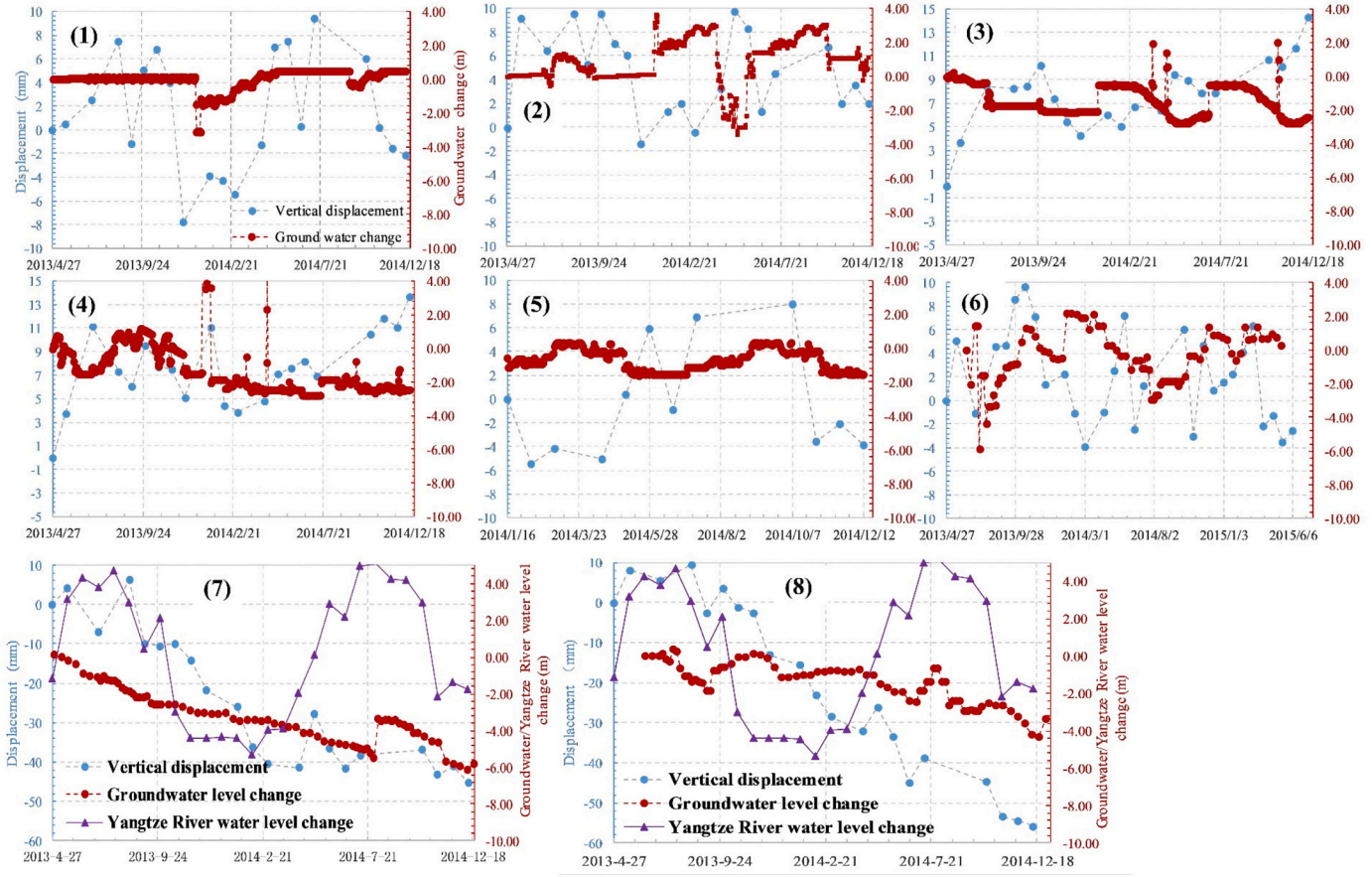


**Fig. 12.** Time series of vertical displacement based on TSX and groundwater level changes at eight wells: (1) Tianyi, (2) Wanjing, (3) Baibuting_1, (4) Baibuting_2, (5) Baibuting_3, (6) Menghu, (7) Jianzhu, and (8) Tazihu, and the Yangtze River water level changes.

**Table 3**
Final subsidence and degree of soft soil consolidation of three subsidence areas in the Hankou zone.

| Subsidence areas | Final Subsidence (mm) | Consolidation degree of soft soil (%) | | | | |
|---|---|---|---|---|---|---|
| | | Subsidence phase | | Stable phase | Accelerated subsidence phase | |
| | | 2013–end | 2014–end | May 2015 | Aug. 2016 | 2017–end |
| Changfeng (T2) | −86.5 | 8.93% | 30.25% | 46.39% | 59.78% | 93.56% |
| Houhu (T4) | −161.3 | 8.20% | 45.27% | 47.54% | 55.26% | 75.37% |
| Xinrong (T6) | −69.1 | −1.93% | 12.49% | 27.16% | 28.58% | 88.57% |

diagonal of Table 2) were greater in number than those of a single factor (the principal diagonal of Table 2). Therefore, the spatial distribution of land subsidence in the Baishazhou-Jiangdi zone was jointly affected by multiple factors rather by a single factor. In addition, the ecological detection results of the top four factors ($X_1$>$X_6$>$X_4$>$X_2$) showed that the factors had no significant differences in explaining the spatial characteristics of land subsidence when combined and exerted positive isotropic effect on the spatial distribution of land subsidence.

### 5.4. Risk assessment to infrastructures

The risk map shown in Fig. 10a, c suggested that the degree of damage caused by land subsidence to civil infrastructure varied noticeably in soft soil areas and karst areas. For example, land subsidence in Hankou and Xudong-Qingshan (HK-XDQS) was the most extensive and severe (Fig. 10a). However, the geological conditions of non-karstic strata and overlying multi-layered soft soil led to land subsidence in the HK-XDQS areas characterized mainly by consolidation mechanisms and large-scale uniform subsidence. At these extent and distribution of land subsidence, moderate deformation gradients with a maximum *SHG* of 1/825 were observed. Thus, only 0.3% of the areas fell in the high-risk zone (1/1500–1/500), and 99.1% of the grids had *SHG* values of less than 1/3000. In contrast, in Baishazhou-Jiangdi zone, localized karst subsidence led to relatively large deformation gradients, and 0.5% of the areas were in the high-risk zone (a cumulative area of 1.04 $km^2$) (Fig. 10a). Different degrees of damage were also found in the risk zoning maps (Fig. 10c); the Level–I and Level–II risk areas were mainly distributed in the Tianxingzhou karst zone and Baishazhou-Jiangdi zone, while the Level–III risk area was generally distributed along the metro lines (Fig. 10b,c).

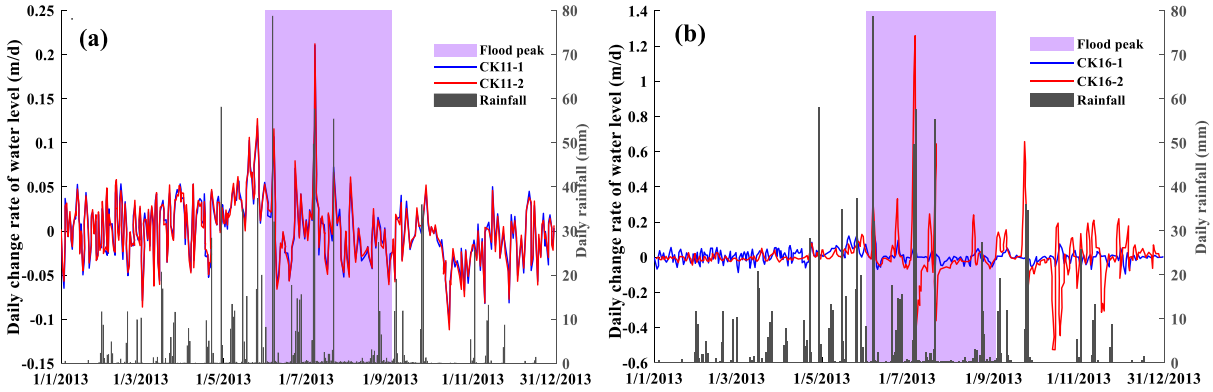


**Fig. 13.** Daily change rates of shallow groundwater (red line) and karst (blue) water level changes during 2013 in (a) Lujiajie Middle School and (b) Fenghuo village. The grey bar represents the daily rainfall in Wuhan. (For interpretation of the references to colour in this figure legend, the reader is referred to the web version of this article.)

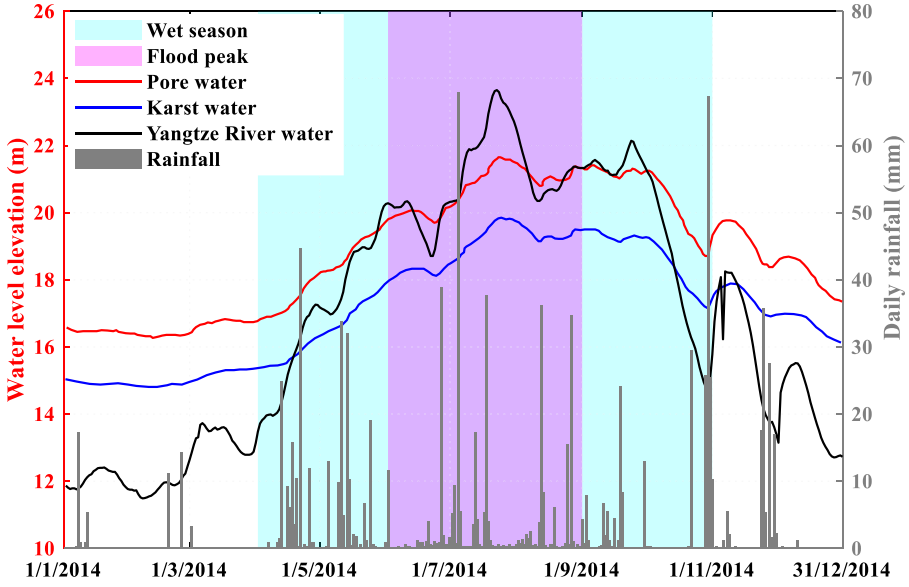


**Fig. 14.** Water level changes and daily rainfall curves at the front edge of the first terrace of the Yangtze River. Wet season: April to October. Flood peak: June to August.

## 6. Conclusion

An integrated analysis using InSAR and hydrgeological measurements resulted in the following conclusions: two governing subsidence mechanisms were observed in Wuhan, namely, soft soil consolidation subsidence in non-karstic soft soil areas and karst subsidence in well-developed karst areas. The Hankou, Xudong-qingshan, and Jianshe-Yangluo zones showed the first mechanism, where land subsidence is positively correlated with groundwater level declines due to engineering dewatering and excessive water depletion from heavy industries.

The second subsidence mechanism was found in the Baishazhou-Jiangdi zone, where three karst zones are distributed. In this well-developed karst area, the downward seepage path between the shallow groundwater and karst water layers is unobstructed, and lateral runoff between shallow groundwater and Yangtze River water is closely linked. Our results from spatial variation analysis of geological conditions suggest the stage of karst development to be the most important factor affecting the spatial distribution of karst subsidence in Wuhan, followed by other factors including proximity to metro lines and construction sites, proximity to major rivers, overlying soil structure, abundance in sediment pore water, and overlying soil thickness. Moreover, we found that the coupling effects from multiple driving factors contributed more to land subsidence than the effect of a single factor. Finally, a quantitative risk mapping indicated that among all regions within Wuhan, civil infrastructures in the Baishazhou-Jiangdi zone and Tianxingzhou karst illustrate the highest level of risk due to land subsidence. Hence, future urban development and management plans in these areas should be taken with care in order to mitigate the risk posed by subsidence hazard to population and infrastructure.

## Author contributions

Conceptualization, J.H. and M.M.; funding acquisition, M.M., J.G., and F.Q.; investigation, J.H., T.L., and W.W.; validation, M.H.H. and M. M.; writing-review & editing, J.H. and M.M. All authors have read and agreed to the published version of the manuscript.

## Declaration of Competing Interest

The authors declare that they have no known competing financial interests or personal relationships that could have appeared to influence the work reported in this paper.

## Acknowledgements

This work was sponsored by the National Natural Science Foundation of China (No. 42174037), Henan Provincial Key R&D and Promotion Special Project (Sci-ence and Technology Research) (No. 212102310414). The TerraSAR-X data were provided by DLR under proposal number GEO1916, and the Copernicus Sentinel data were provided by ESA. We would like to thank Hubei Geological Environmental Center for providing abundant geological dataset and karst survey reports. We are especially grateful to Janusz Wasowski and the anonymous reviewers for their valuable comments, which greatly improved the quality of this manuscript.

## References

Bagheri-Gavkosh, M., Hosseini, S.M., Ataie-Ashtiani, B., Sohani, Y., Ebrahimian, H., Morovat, F., Ashrafi, S., 2021. Land subsidence: a global challenge. Sci. Total Environ. 2021 (778), 146193.

Bai, L., Jiang, L.M., Wang, H.S., Sun, Q.S., 2017. Spatiotemporal characterization of land subsidence and uplift (2009–2010) over Wuhan in Central China revealed by TerraSAR-X InSAR analysis. Remote Sens. 8, 350.

Bekaert, D., Walters, R., Wright, T., Hooper, A., Parker, D., 2015. Statistical comparison of InSAR tropospheric correction techniques. Remote Sens. Environ. 170, 40–47.

Berardino, P., Fornaro, G., Lanari, R., Sansosti, E., 2002. A new algorithm for surface deformation monitoring based on small baseline differential SAR interferograms. IEEE Trans. Geosci. Remote Sens. 40 (11), 2375–2383.

Bonetto, S., Fiorucci, A., Fornaro, M., Vigna, B., 2008. Subsidence hazards connected to quarrying activities in a karst area: the case of the Moncalvo sinkhole event (Piedmont, NW Italy). Estonian J. Earth Sci. 57, 125–134.

Cigna, F., Tapete, D., 2021. Present-day land subsidence rates, surface faulting hazard and risk in Mexico City with 2014–2020 Sentinel-1 IW InSAR. Remote Sens. Environ. 253, 1–19.

Dahm, T., Kühn, D., Ohrnberger, M., Kröger, J., Wiederhold, H., Reuther, C.-D., Dehghani, A., Scherbaum, F., 2010. Combining geophysical data sets to study the dynamics of shallow evaporites in urban environments: application to Hamburg, Germany. Geophys. J. Int. 181, 154–172.

Fernández-Torres, E., Cabral-Cano, E., Solano-Rojas, D., Havazli, E., Salazar-Tlaczani, L., 2020. Land Subsidence risk maps and InSAR based angular distortion structural vulnerability assessment: an example in Mexico City. Proc. Int. Assoc. Hydrol. Sci. 382, 583–587.

Ferretti, A., Prati, C., Rocca, F., 2001. Permanent scatterers in SAR interferometry. IEEE Trans. Geosci. Remote Sens. 39 (1), 8–20.

Galve, J.P., Castañeda, C., Gutiérrez, F., Herrera, G., 2015. Assessing sinkhole activity in the Ebro Valley mantled evaporite karst using advanced DInSAR. Geomorphology 229, 30–44.

Ge, S.P., Liao, S.M., Chen, L.S., Chen, D.X., 2008. Influence of construction and operation of metro tunnel on settlement of ground buildings and countermeasures. Chin. J. Rock Mech. Eng. 27 (03), 550–556. https://doi.org/10.3321/j.issn:1000-6915.2008.03.015 (in Chinese).

Gutiérrez, F., Galve, J.P., Lucha, P., Cadtañeda, C., 2012. Integrating geomorphological mapping, trenching, InSAR and GPR for the identification and characterization of sinkholes: a review and application in the mantled evaporate karst of the Ebro Valley (NE Spain). Geomorphology 134, 144–156.

Haghshenas Haghighi, M., Motagh, M., 2019. Ground surface response to continuous compaction of aquifer system in Tehran, Iran: results from a long-term multi-sensor InSAR analysis. Remote Sens. Environ. 221, 534–550.

Han, Y., Zou, J., Lu, Z., Qu, F., Kang, Y., Li, J., 2020. Ground deformation of Wuhan, China, revealed by multi-temporal InSAR analysis. Remote Sens. 12 (22), 3788.

He, K., Zhang, S., Wang, F., Du, W., 2010. The karst collapses induced by environmental changes of the groundwater and their distribution rules in North China. Environ. Earth Sci. 61 (5), 1075–1084.

Herrera-García, G., Ezquerro, P., Tomás, R., Béjar-Pizarro, M., López-Vinielles, J., Rossi, M., Ye, S., 2021. Mapping the global threat of land subsidence. Science. 371 (6524), 34–36.

Hooper, A., Segall, P., Zebker, H., 2007. Persistent scatterer InSAR for crustal deformation analysis, with application to Volcán Alcedo, Galapagos. J. Geophys. Res. 112, 1–19.

Jia, L., Li, L., Meng, Y., Wu, Y., Pan, Z., Yin, R., 2018. Responses of cover-collapse sinkholes to groundwater changes: a case study of early warning of soil cave and sinkhole activity on Datansha Island in Guangzhou, China. Environ. Earth Sci. 77 (13), 1–11.

Jiang, H., Balz, T., Cigna, F., Tapete, D., 2021. Land subsidence in Wuhan revealed using a non-linear PSInSAR approach with long time series of COSMO-SkyMed SAR data. Remote Sens. 13 (7), 1256.

Kampes, B.M., Hanssen, R.F., Perski, Z., 2003. Radar interferometry with public domain tools. In: Proceedings of FRINGE 2003, Frascati, Italy.

Kim, J.-W., Lu, Z., Kaufmann, J., 2019. Evolution of sinkholes over Wink, Texas, observed by high-resolution optical and SAR imagery. Remote Sens. Environ. 222, 119–132.

Luo, X.J., 2013. Features of the shallow karst development and control of karst collapse in Wuhan. Carsol. Sin. 32 (4), 419–432 (in Chinese).

Motagh, M., Djamour, Y., Walter, T.R., Wetzel, H.U., Zschau, J., Arabi, S., 2007. Land subsidence in Mashhad Valley, Northeast Iran: results from InSAR, levelling and GPS. Geophys. J. Int. 168 (2), 518–526.

Motagh, M., Walter, T.R., Sharifi, M.A., Fielding, E., Schenk, A., Anderssohn, J., Zschau, J., 2008. Land subsidence in Iran caused by widespread water reservoir overexploitation. Geophys. Res. Lett. 35, L16403. https://doi.org/10.1029/2008GL033814.

Motagh, M., Shamshiri, R., Haghighi, M.H., Wetzel, H.U., Akbari, B., Nahavandchi, H., Arabi, S., 2017. Quantifying groundwater exploitation induced subsidence in the Rafsanjan plain, southeastern Iran, using InSAR time-series and in situ measurements. Eng. Geol. 218, 134–151.

Ng, A.H.M., Wang, H., Dai, Y., Pagli, C., Chen, W., Ge, L., Du, Z., Zhang, K., 2018. InSAR reveals land deformation at Guangzhou and Foshan, China between 2011 and 2017 with COSMO-SkyMed data. Remote Sens. 10, 813.

Orhan, O., Oliver-Cabrera, T., Wdowinski, S., Yalvac, S., Yakar, M., 2021. Land subsidence and its relations with sinkhole activity in Karapınar region, Turkey: a multi-sensor InSAR time series study. Sensors. 21 (3), 774.

Park, S., Hong, S., 2021. Nonlinear modeling of subsidence from a decade of InSAR time series. Geophys. Res. Lett. 48 (3) https://doi.org/10.1029/2020gl090970.

Perkins, S., 2021. Core Concept: often driven by human activity, subsidence is a problem worldwide. Proc. Natl. Acad. Sci. 118, 20.

Qu, F., Zhang, Q., Lu, Z., Zhao, C., Yang, C., Zhang, J., 2014. Land subsidence and ground fissures in Xi'an, China 2005–2012 revealed by multi-band InSAR time-series analysis. Remote Sens. Environ. 155, 366–376.

Shi, Y., Tang, Y., Lu, Z., Kim, J.W., Peng, J., 2019. Subsidence of sinkholes in Wink, Texas from 2007 to 2011 detected by time-series InSAR analysis. Geomat. Nat. Hazard Risk 10 (1), 1125–1138.

Skempton, A.W., Macdonald, D.H., 1956. The allowable settlements of buildings. Proc. Inst. Civ. Eng. 5, 727–768.

Sun, H., Zhang, Q., Zhao, C., Yang, C., Sun, Q., Chen, W., 2017. Monitoring land subsidence in the southern part of the lower Liaohe plain, China with a multi-track PS-InSAR technique. Remote Sens. Environ. 188, 73–84.

Terzaghi, K., Peck, R.B., Mesri, G., 1996. Soil Mechanics in Engineering Practice. John Wiley & Sons, New York.

Tomás, R., Herrera, G., Lopez-Sanchez, J.M., Vicente, F., Cuenca, A., Mallorquí, J.J., 2010. Study of the land subsidence in Orihuela City (SE Spain) using PSI data: distribution, evolution and correlation with conditioning and triggering factors. Eng. Geol. 115, 105–121.

Wang, Y., Merkel, B.J., Li, Y., Ye, H., Fu, S., Ihm, D., 2007. Vulnerability of groundwater in Quaternary aquifers to organic contaminants: a case study in Wuhan City, China. Environ. Geol. 53 (3), 479–484.

Wang, J.F., Li, X.H., Christakos, G., Liao, Y.L., Zhang, T., Gu, X., Zheng, X.Y., 2010. Geographical detectors-based health risk assessment and its application in the neural tube defects study of the Heshun Region, China. Int. J. Geogr. Inf. Sci. 24 (1), 107–127.

Wang, X., Lai, J., He, S., Garnes, R.S., Zhang, Y., 2020. Karst geology and mitigation measures for hazards during metro system construction in Wuhan, China. Nat. Hazards 103 (3), 2905–2927.

Werner, C., Wegmüller, U., Strozzi, T., Wiesmann, A., 2000. Gamma SAR and interferometric processing software. In: Proceedings of the ERS-Envisat Symposium, Gothenburg, Sweden.

Xu, G.L., 2016. Mechanism Study and Hazard Assessment of Covered Karst Sinkholes in Wuhan City, China. PHD thesis. China University of Geosciences, Wuhan, China (in Chinese).

Yu, C., Li, Z., Penna, N.T., Crippa, P., 2018. Generic atmospheric correction model for interferometric synthetic aperture radar observations. J. Geophys. Res. Solid Earth 1–21. https://doi.org/10.1029/2017JB015305.

Zhang, Y., Liu, Y., Jin, M., Jing, Y., Liu, Y., Liu, Y., Chen, Y., 2019. Monitoring land subsidence in Wuhan city (China) using the SBAS-InSAR method with radarsat-2 imagery data. Sensors 19 (3), 743.

Zhou, L., Guo, J.M., Hu, J.Y., Li, J.W., Xu, Y.F., Pan, Y.J., Shi, M., 2017. Wuhan surface subsidence analysis in 2015–2016 based on Sentinel-1A data by SBAS-InSAR. Remote Sens. 9, 982.

Zhu, L., Gong, H., Li, X., Wang, R., Chen, B., Dai, Z., Teatini, P., 2015. Land subsidence due to groundwater withdrawal in the northern Beijing plain, China. Eng. Geol. 193, 243–255.